

IN12-XXXXX

VIBROACOUSTIC CHARACTERIZATION OF A NEW HYBRID WING-BODY FUSELAGE CONCEPT

Albert Allen

Structural Acoustics Branch
NASA Langley Research Center
Hampton, VA 23681
Email: albert.r.allen@nasa.gov

Adam Przekop

Analytical Services & Materials, Inc.
Hampton, VA 23666
Email: adam.przekop@nasa.gov

ABSTRACT

A lighter, more robust airframe design is required to withstand the loading inherent to next generation non-cylindrical commercial airliners. The Pultruded Rod Stitched Efficient Unitized Structure concept, a highly integrated composite design involving a stitched and co-cured substructure, has been developed to meet such requirements. While this structure has been shown to meet the demanding out-of-plane loading requirements of the flat-sided pressurized cabin design, there are concerns that the stiff co-cured details will result in relatively high acoustic radiation efficiencies at frequencies well below the thin skin acoustic coincidence frequency. To address this concern and establish a set of baseline vibroacoustic characteristics, a representative test panel was fabricated and a suite of tests were conducted that involved measurements of panel vibration and radiated sound power during point force and diffuse acoustic field excitations. Experimental results are shown and compared with Finite Element and Statistical Energy Analysis model predictions through the use of modal and energy correlation techniques among others. The behavior of the structure subject to turbulent boundary layer excitation is also numerically examined.

INTRODUCTION

NASA has created the Environmentally Responsible Aviation (ERA) Project to explore the feasibility, benefits, and technical risk of advanced vehicle configurations and enabling technologies that will reduce the impact of aviation on the environment. A critical aspect of this pursuit is the development of a lighter, more robust airframe that will enable the introduction of

unconventional aircraft configurations, such as the hybrid wing-body (HWB) as depicted in figure 1.

The primary structure concept being developed under the ERA Airframe Technology element is the Pultruded Rod Stitched Efficient Unitized Structure (PRSEUS) concept. The PRSEUS construction (figure 2) utilizes an integral one-piece design approach with co-cured details that are joined together by stitching to provide exceptional out-of-plane strength and improved damage tolerance. Although the resulting structure has been shown to meet the demanding out-of-plane loading requirements of the HWB flat-sided pressure cabin design, there are concerns that the lighter, stiffer, co-cured details of composite fuselage structures such as PRSEUS could provide higher sound transmission to the cabin interior than that exhibited by conventional metallic fuselage structures flying today. To address these concerns, and to establish a baseline set of acoustic characteristics for a PRSEUS panel, an acoustic test panel was designed and fabricated by The Boeing Company and subsequently delivered to NASA LaRC for testing. The test panel design was based on the HWB minimum gauge pressure cabin panel geometry established during the NASA NRA Phase I trade studies and then structurally tested during the Phase II portion of the program [1].

The goal of the experimentation conducted at NASA LaRC was to validate numerical models of the baseline PRSEUS configuration, which include finite element (FE) and statistical energy analysis (SEA) models. In order to incorporate both the structural vibration and sound radiation behavior of the structure in the validation effort, a variety of tests were conducted including loss factor estimation, low frequency modal correlation, mid to high frequency bay energy correlations, diffuse acoustic field

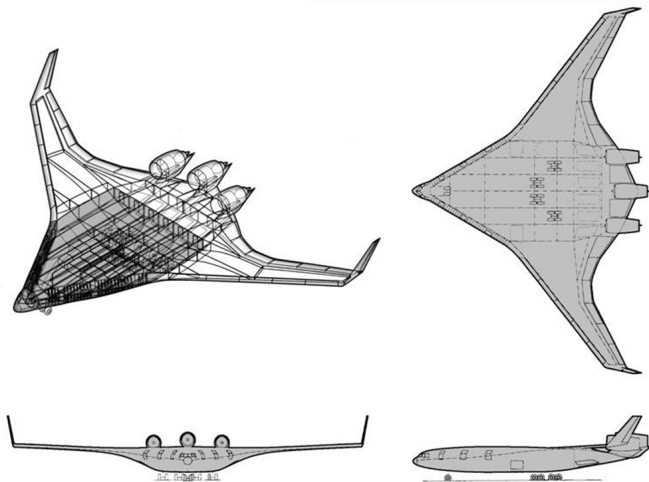


FIGURE 1. Hybrid wing-body concept.

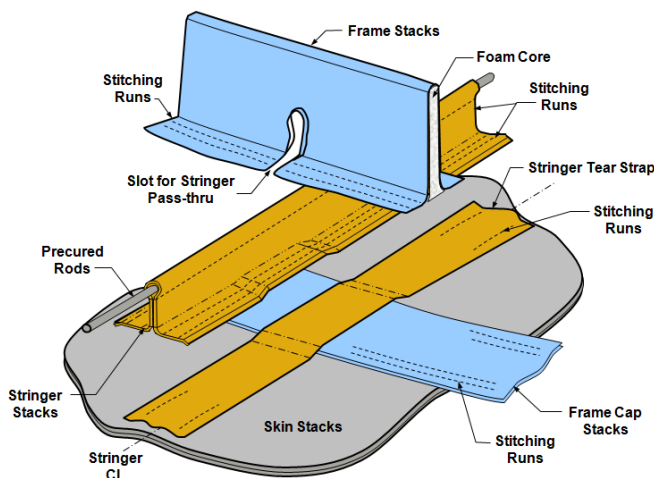


FIGURE 2. PRSEUS concept.

(DAF) transmission loss (TL), and sound radiation due to point excitation. Once validated, the models (or a subset thereof) will be used to evaluate modifications that may result in improved vibroacoustic performance of the primary structure early in the design stage, thus reducing the need for additional mass in the form of late design stage noise treatments.

The paper begins with a description of the baseline test structure followed by a description of the numerical models. The test methods, data reduction techniques, and results are then described and compared with model predictions. Finally, a candidate design modification is evaluated under representative flight conditions.

TEST STRUCTURE

The 1.22 m×1.22 m test structure under study is shown in figure 3. The panel consists of carbon composite skin and substructure components that were stitched in place, bagged, vacuum resin infused, and then cured using an out-of-autoclave process [1]. The laminae used in the structure were of Class 72 Type I warp-knit fabric arrangements comprised exclusively of AS-4 (or equivalent intermediate modulus) carbon fibers. The nominal laminate used in the structure consisted of a 7 ply stack, $[45^\circ, -45^\circ, 0^\circ, 90^\circ]_S$, where the 0° laminae were approximately twice as thick as the 45° laminae giving fiber area weight percentages of 45%, 43%, and 12% for the 0° , 45° , and 90° layers, respectively. The skin was comprised of a single layer of this orthotropic stack, the material properties of which are provided in table 1, while multiple layers were used for the frame and stringer overwraps as shown in table 2. For reference, the direction of higher modulus in the single stack skin was parallel with the frames. Additional pad-ups were applied near the perimeter of the panel to facilitate handling. The frames (figure 5(a)) were spaced 61 cm apart and consist of a 12.7 mm thick Rohacell 110WF foam core with an overwrap of two stacks. The overwrap was pinched near the top of the frame to increase static bending stiffness. The stringers (figure 5(b)) were spaced 15.2 cm apart and consisted of a 9.5 mm diameter carbon fiber pultruded rod with a single stack overwrap. The pultruded rod was tapered on one side to produce an inverted tear drop shape conforming with the overwrap bend radii at the top of the stringer web. At each frame and stringer intersection, the frame was notched to allow the stringer to pass through. These junction regions were fully infused with adhesive and did not exhibit open “mouse holes”. There were no fasteners in this structure.

A portion of the testing required the panel to be installed in the Structural Acoustics Loads and Transmission (SALT) facility, a schematic of which is shown in figure 4. The SALT test facility is further described in [2, 3]. A sandwich adaptor frame comprised of 50 mm thick medium density fiberboard core bonded between two 6.35 mm thick aluminum face sheets was constructed to mate the panel with the existing SALT facility window. The panel was machined to a thickness of 3.7 mm along

TABLE 1. Single stack laminate properties.

E_{11}	67.2 GPa
E_{22}	33.5 GPa
ν_{12}	0.40
ρ	1578 kg/m ³
G_{12}	16.3 GPa
thickness	1.32 mm

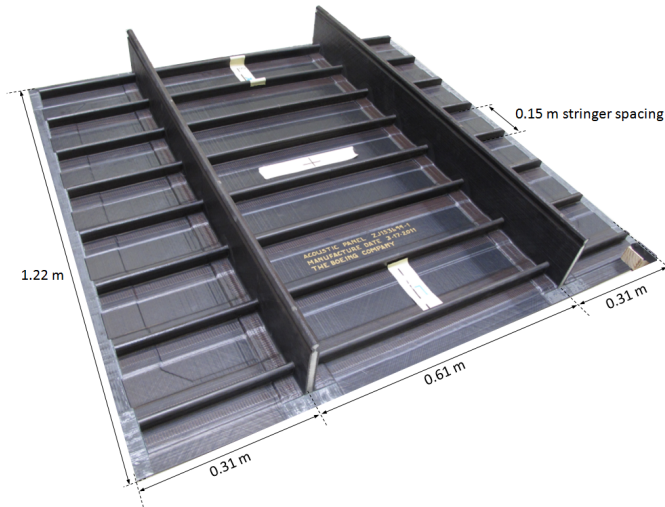


FIGURE 3. Baseline configuration test structure.

a 25.4 mm wide perimeter, which was sandwiched to the adaptor frame with 6.35 mm thick aluminum clamping bars. The clamping bars were overlapped at the corners to avoid discontinuities in the boundary condition (BC). Substructure components were truncated at the inner clamped perimeter edge to avoid strong coupling to the test fixture in the frequency range of concern. A Visual Image Correlation (VIC) scan of the test panel was completed prior to testing and indicated a slight panel warping due to residual thermal stresses introduced in the curing process. To avoid additional pre-stress conditions, a detailed layered shim was constructed based on the VIC measurements and applied at the panel perimeter. During in-situ test conditions, the panel and clamping bar components were fastened to the adaptor frame with 44 9.5 mm diameter bolts uniformly spaced 10 cm apart and torqued to 20 m-N.

NUMERICAL MODELS

A combination of deterministic FE and SEA approaches were used to model the vibroacoustic behavior of the baseline PRSEUS configuration in the frequency range of interest, namely the Speech Interference Level (SIL) octave bands. An FE model allows for the explicit modeling of structural details that could be important from a quiet design perspective, such as the frame and stringer flanges, while an SEA model allows for faster run times at higher frequencies or for larger models precluding a FE approach.

The FE model, shown in figure 6, was developed using the commercially available Abaqus. The model was discretized primarily with S4R rectangular shell elements representing the skin, flanges, webs, and frame overwraps, while the frame core and

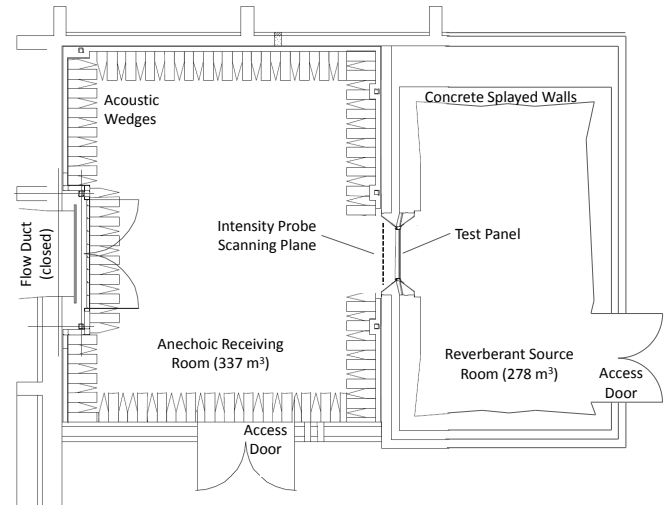


FIGURE 4. Schematic of SALT facility.

pultruded rods were modeled using C3D8 solid and B31 beam elements, respectively. One stack comprising seven individual plies was modeled as a single layer in the shell element property definition. Nominal values of thickness and material properties were used per tables 1 and 2 with an exception of composite density, which was reduced by 3.5% from the nominal to match the measured mass of the panel. Through-thickness stitching was not modeled explicitly as this level of fidelity was thought unnecessary for the purposes of the model. The typical element size was selected to resolve the smallest flexural waves adequately up to the 3.15 kHz 1/3 octave band. Consequently, an element edge size of approximately 12 mm was selected, which corresponds to approximately 5 elements per wavelength at the thinnest single-stack sections of the skin in the direction of least tensile stiffness. To provide a smooth Outer-Mold-Line (OML) contour of the panel, element mid-thickness offsets from a planar node surface definition were used in the modeling effort.

The panel was tested in two distinct BCs 1) suspended on two bungee cords attached to its top edge along the frame lines (free hanging), and 2) installed in the SALT TL window by fastening the panel perimeter to an adaptor frame, also referred to as *in situ*. Unconstrained BCs were applied in the FE analysis to approximate the free hanging situation, while idealized clamped BCs were applied along the panel perimeter to approximate the *in situ* BC.

While a VIC scan of the test panel was available and indicated a slight panel warping due to residual thermal stresses introduced in a curing process, such an imperfection was not modeled. Modeling of an initial pre-stress condition for the clamped BC case was also deemed unnecessary as a detailed shim was manufactured based on the VIC measurements and applied to minimize the impact of geometry imperfection.

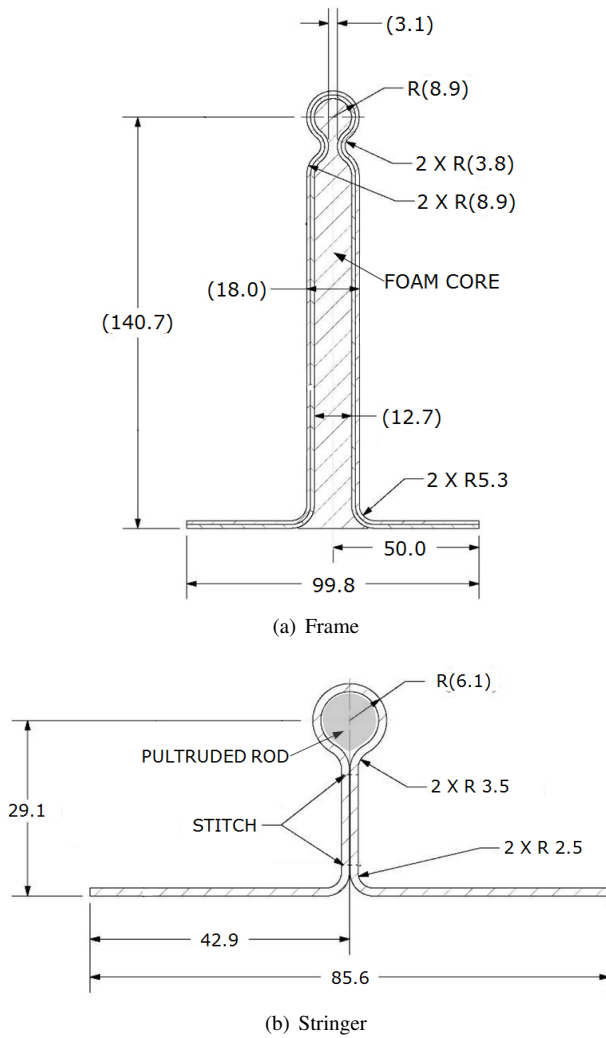


FIGURE 5. Baseline configuration substructure cross section details (mm).

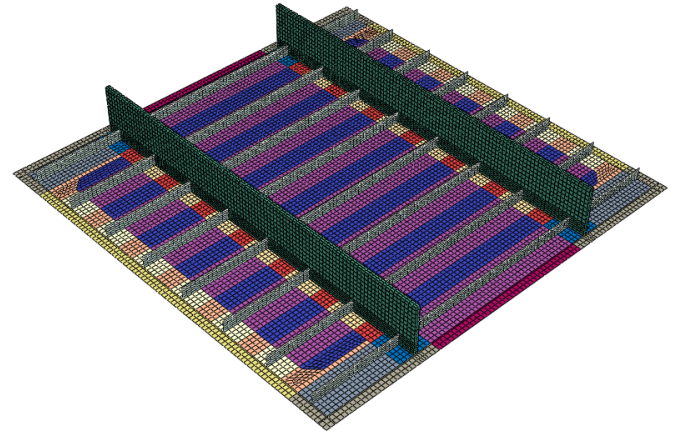


FIGURE 6. FE model of test structure.

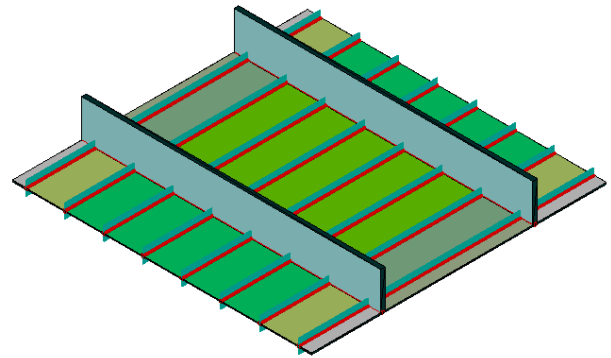


FIGURE 7. SEA model of test structure.

The use of FEM above the 3.15 kHz 1/3 octave band, while possible, was thought to be prohibitive due to the large number of degrees of freedom required to avoid spatial aliasing at higher frequencies. Consequently, SEA, an energy diffusion modeling approach requiring significantly fewer degrees of freedom, was preferred at higher frequencies. In a SEA model, the structure is

TABLE 2. Test structure stack sequences and orientations.

Component	Stack Orientation (0° parallel with stringers)	Thickness (mm)
Skin	[90°]	1.32
Frame Flange	[90°, 90°] _S	5.28
Stringer Flange	[90°, 0°, 0°]	3.96
Frame/Stringer Intersection Flange	[90°, 90°, 0°] _S	7.93
Frame Web	[0°, 0°, foam, 0°, 0°]*	17.98
Stringer Web	[0°] _S	2.64

*0° parallel with frames

represented as a collection of subsystems, which are regions of similar modes typically partitioned along junctions of significant impedance mismatch. The subsystem acts as a single degree of freedom representing the energy content for a given wavetype, e.g. a bay of the test structure described here would be modeled as a plate subsystem with three degrees of freedom representing the energy content due to flexural, extensional, and shear wavytypes. The model is then perturbed by power inputs to one or more subsystems and the resulting energy diffusion depends on power transmission at junctions and dissipation within subsystems. ESI Group's VAOne software was used to develop the SEA model of the baseline PRSEUS panel as shown in figure 7. The FE model geometry and preliminary eigenanalysis results largely facilitated the SEA model development. The structure was partitioned into bays modeled as separate orthotropic plate subsystems, stringer segments between frames as beam subsystems, and frames as general laminate plates. The substructure flanges posed an exceptional difficulty from an SEA modeling standpoint. In this study, the flange details were "smeared" into uniform bay subsystems by using area weighted averages of the thicknesses and orthotropic material properties. The coupling loss factors assigned by the solver were used, i.e. these parameters were not updated with experimental data. The damping loss factors, which are a measure of the energy dissipation within a subsystem, were, however, estimated experimentally as described in the following section.

EXPERIMENTAL

A suite of tests were conducted to facilitate model development and validation. Initially, the panel was placed in a free hanging, un baffled boundary condition in the SALT anechoic chamber to measure the structural response under a series of point excitations. The free hanging boundary condition provided a simple way to avoid confounding boundary condition effects while correlating the models. Normal velocity measurements were taken along the OML side of the panel with a Polytec OFV-056 scanning laser vibrometer while the structure was point excited with a Brüel & Kjær Type 4809 shaker situated in a trunnion. Force and acceleration signals were acquired with a PCB 288D01 impedance head to resolve the drive point mobility and power input at a given excitation location. A series of 5 and 3 excitation points were chosen at Inner-Mold-Line (IML) (substructure side) locations within bays numbered 5 and 12, respectively, (see figure 10) to provide power input and bay energy statistics. Periodic chirp excitations were used to reduce the amount of block averaging required for frequency response function (FRF) convergence during the scans and to avoid introducing time windowing effects. Acquisition periods of 3.2, 0.64, and 0.16 seconds were used for 0-500 Hz, 500-5000 Hz, and 5000-10000 Hz frequency range scans, respectively, to reduce the test time at the higher frequencies while fully including

the panel reverberation within the acquisition period at the lower frequencies. Dividing the scans in this way also made it easier to adequately excite the structure, which yielded agreeable point and transfer mobility FRF coherences at all locations and frequencies. The scan grid captured the extents of the OML side of the panel with a spatial resolution of approximately 25 mm, which resolved the wavelength up to at least 1 kHz for modal correlation purposes. At higher frequencies, the same grid resolution was thought adequate to distinguish the normal velocity at a given scan point mass, m_n , for calculating bay energy content and to provide an adequate number of transfer FRFs for damping estimation.

Further in situ tests were conducted while the panel was installed in the SALT TL window. The panel was shimmed along the perimeter prior to fastening into a massive adaptor frame with the IML side facing the anechoic chamber and frames running vertically. Excitation locations and vibrometer scan procedures used in the free hanging condition were repeated for the in situ condition, although the 4809 trunnion mounted shaker was replaced with a free hanging Brüel & Kjær Type 4810 mini shaker to avoid interactions between the shaker assembly and constrained panel. The panel's point excited radiated sound powers from IML and OML sides were also measured by using intensity scan [4] and direct room acoustic methods, respectively. The intensity probe array setup in SALT consisted of a vertical array of 5 equidistantly spaced intensity probes (Brüel & Kjær Type 2683 pre-amplifiers with Type 4197 microphone pairs) able to traverse horizontally and vertically under software control. The intensity probe measurement plane was offset from the panel skin by approximately 36 cm and extended to the 45 degree walls surrounding the aperture to fully enclose the structure's radiation path. The offset distance was dictated by the physical constraints of the array traverse system and the desire to avoid any highly reactive fields close to the radiating surface. The intensity probe array grid spacing was set to, at most, 14 cm during testing. In the adjacent reverb chamber, the space averaged mean square pressure was concurrently measured with 12 distributed GRAS Type 40AQ 1/2 inch pre-polarized random-incidence microphones with 26CA preamps. Following the sound radiation tests, the shaker assembly was removed and the reverb chamber was ensonified with an array of drivers for a DAF TL test. The chosen scan grid offset distance, grid densities, and signal processing parameters during these tests were found to be adequate through convergence studies prior to final runs.

MODEL CORRELATION

The damping of the panel was estimated using mobility FRFs from vibrometer scans acquired while the panel was situated in free hanging and in situ boundary conditions and shaker point excited at 8 locations separately. Low frequency mode based total loss factors (TLFs) were estimated using the modal

curve fitting module within m+p's SO Analyzer. In the 630 Hz and above 1/3 octave bands, the Impulse Response Decay Method (IRDM) was used to estimate band averaged total loss factors (TLFs) [5]. A follow up IRDM experiment was made using an instrumented hammer to check for bias due to shaker attachment and no significant differences were found.

The loss factors applied to the panel in the models were conditioned depending on the particular model. In a previous study it was suggested that IRDM SEA damping loss factor (DLF) estimates depend on the locations of the response points relative to the force input included in the analysis [6]. When using transfer mobilities with response points located in the same bay subsystem as the applied force, the apparent loss factor estimate tended to approach the assigned DLF at high frequencies. Given this, the high frequency asymptote of the IRDM TLF estimates using transfer mobility FRFs within the driven bay were assigned as DLFs in the SEA models described in this document. Conversely, the loss factors used in the FE modal models were associated with the band averaged "modal" loss factor, so frequency dependant TLF estimates using all transfer mobility FRFs were used in these cases. The results from both boundary conditions are given in figure 8.

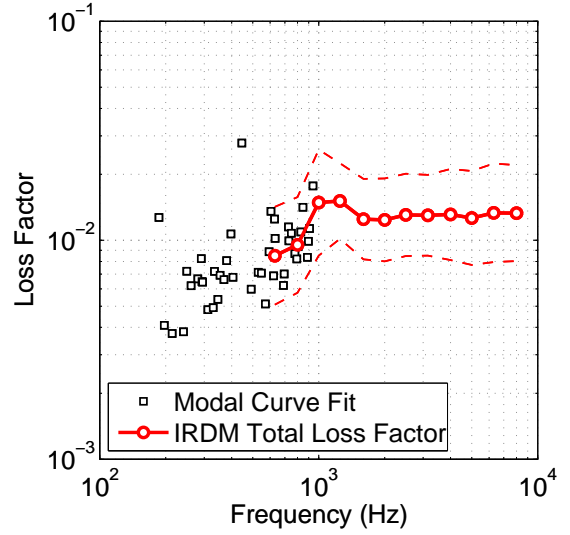
For TL predictions, a vibroacoustic FE model was used that accounted for the acoustic impedance present on both sides of the panel. The structural damping used in this case was found by subtracting the estimated radiation losses from the IRDM TLFs. An experimental SEA approach was taken where the radiated sound power from both sides of the panel is expressed as

$$P_{rad-tot} = \omega \eta_{rad} E_p, \quad (1)$$

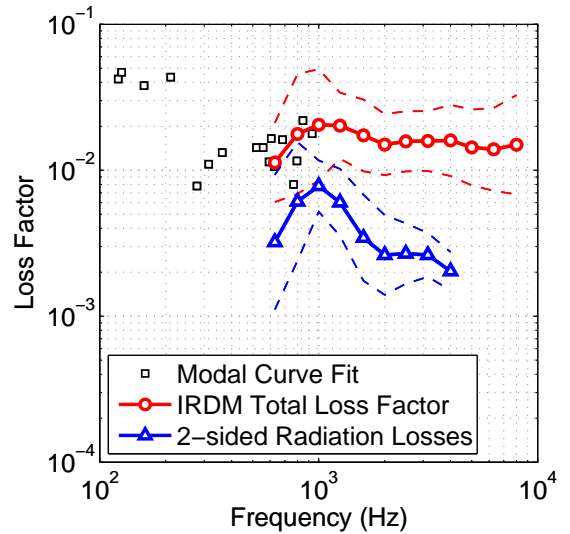
where $E_p = \sum_{n=1}^N m_n \overline{v_n^2}$ and m_n and $\overline{v_n^2}$ are the nodal mass and normal mean square velocity, respectively, at the n^{th} of N vibrometer scan nodes. Scan nodal masses, m_n , were approximated by projecting the FE model nodal masses of the in-plane elements onto the experimental scan grid and then scaling to ensure conservation of mass. The direct room acoustic method was used to estimate the OML side (facing the reverb chamber) radiated sound power [7]. Here, the power absorbed P_{abs} in a room of volume V and absorption area A_{abs} during steady state shaker excitation serves as an estimate of the radiated sound power,

$$P_{rad-room} = P_{abs} \approx \frac{\langle p^2 \rangle A_{abs}}{4\rho_0 c_0} \approx \frac{\langle p^2 \rangle V}{\rho_0 c_0^2} \left(1 + \frac{S_r \lambda}{8V} \right) \frac{13.8}{T_{60}}, \quad (2)$$

where $\langle p^2 \rangle$ is the measured space averaged mean square pressure, S_r is the total surface area of reverb chamber, λ is the acoustic wavelength, and T_{60} is the 60 dB reverberation time (determined using measured T_{20} early decay times from [3]). The panel's IML side (facing the anechoic chamber) radiated sound



(a) Free hanging BC



(b) In situ BC

FIGURE 8. Experimental TLF estimates from low frequency modal curve fits and 1/3 octave IRDM results for free hanging and in situ BCs. The 2-sided radiation loss estimate is also shown for the in situ BC. Dashed lines denote 95/50 confidence intervals.

power was estimated with the intensity probe array,

$$P_{rad-int} = \sum_{k=1}^K I_k S_k, \quad (3)$$

where I_k is the intensity measured at the k^{th} of K intensity probe scan locations, each having a respective scan area S_k . The radiated sound powers from both sides of the panel were combined in $P_{rad-tot}$ to provide the 2-sided radiation losses, η_{rad} . Only the normal velocity of the skin measured from the OML side was used to estimate E_p , i.e. frame and stringer responses were not included. The substructure mass content was, however, added into the nodal masses, m_n , along the frame and stringer lines, although this attribution was largely insignificant as the regions along the substructure lines exhibited low normal velocities once the local bay modes were cut-on. Power feedback into the panel from the reverb chamber was initially considered, but found insignificant with regard to the estimated radiation losses and was not accounted for in equation 1. Radiation loss factor results above the 4 kHz 1/3 octave band were removed due to poor S/N ratio precluding the use of reverb chamber mean square pressure data in equation 2.

The measured normal velocity of the panel under point excitation, \mathbf{V}_{exp} , was then compared with FE predictions, \mathbf{V}_{fe} , on a modal basis in the lower frequencies using Modal Assurance Criterion (MAC) correlations of the velocity response shapes at frequencies (p, q) near resonance,

$$MAC_{exp,fe} = \frac{|\mathbf{V}_{exp}^T \mathbf{V}_{fe}|^2}{(\mathbf{V}_{exp}^T \mathbf{V}_{exp}) (\mathbf{V}_{fe}^T \mathbf{V}_{fe})}, \quad (4)$$

where T signifies a matrix transpose and \mathbf{V} is an $N \times 1$ matrix representing the velocity response at N nodes. The test scan grid resolution was approximately half that of the FE model, so the FE results were interpolated to the scan grid locations prior to calculating MAC values. Modal curve fit damping estimates were used in the FE model as described previously, although the MAC correlations were found to be insensitive to this parameter. A pseudo-heuristic approach was taken when determining comparable response shapes at resonance and involved both subjective shape comparison and searching along neighboring frequencies for shapes of highest correlation. Relative frequency error between test and FE resonant responses and their respective shape MAC values are shown in figure 9 for free hanging (modeled with an unconstrained perimeter) and in situ (modeled with a clamped perimeter) boundary conditions. The free hanging MAC correlations show good agreement for the first few modes above which the modal overlap tends to increase and the correlations begin to diverge. There is also no significant frequency bias in the unbound model, which suggests that the mass and stiffness distribution of the structure was adequately represented.

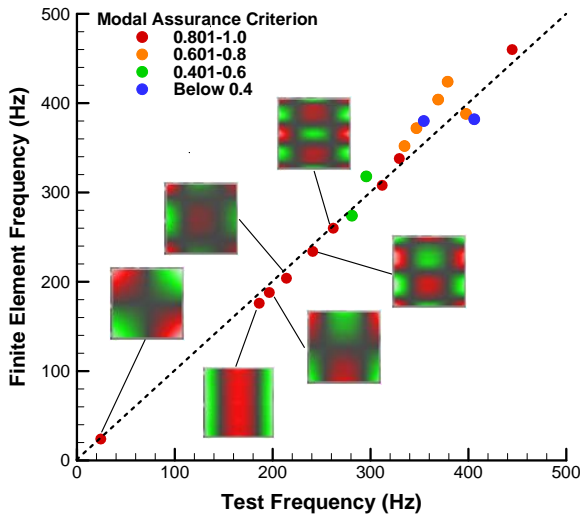
The in situ test results had relatively lower modal overlap in the lower frequencies, which allowed correlations to be made up to ~ 1 kHz above which the number of bay modes increased substantially. The frequency bias shown suggests a slightly over-

stiff model, which was attributed to the use of idealized clamped boundary conditions instead of explicitly modeling the adaptor frame and facility window. To investigate the in situ BC further, a FE model of the adaptor frame was developed, experimentally validated, and then added to the panel FE model. It was found that there was no significant difference in the panel eigenfrequencies between the ideally clamped panel and the panel coupled with the ideally clamped adaptor frame, which suggests that the BC presented at the interface between the adaptor frame and facility window was the remaining unknown. As the frequency bias was thought to be small and because further modeling of the facility window was thought to be outside the scope of this effort, idealized clamped BCs along the panel perimeter were retained in the FE model. Consequently, some of the measured in situ modes below ~ 200 Hz exhibited strong coupling with the surrounding structures and were not represented well in the model if at all. The high TLF estimates from figure 8 below ~ 200 Hz are also characteristic of modes strongly coupled to the surrounding structure. These low frequency facility interactions were noted, but were generally thought of as being outside the frequency range of interest.

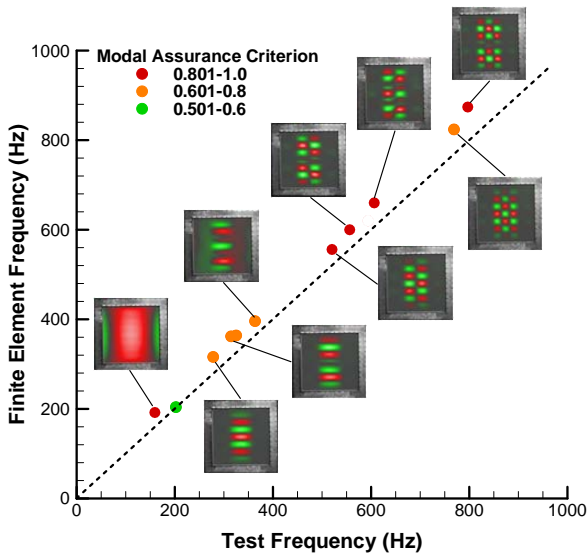
An energy correlation technique was then used to validate the models against test results at higher frequencies where the modal overlap precluded correlation on a modal basis. Vibrometer scan and impedance head data taken during 8 separate drive point excitations as previously mentioned were used to determine bay energy content relative to power input $E_y/P_{in,x}$. Here, E_y represents the bay energy content and was calculated as in equation 1 while constraining the node sets to include only regions within the y^{th} bay not including nodes within direct proximity to the frame and stringer webs. Point load power inputs applied within the x^{th} bay were determined from

$$P_{in,x} = \overline{F_0^2} \text{Re}\{Y_{00}\}, \quad (5)$$

where $\overline{F_0^2}$ and Y_{00} are the collocated mean square force and drive point mobility, respectively. Only the mass contribution of the in-plane panel components were accounted for when determining bay energy content. The energy and power values as well as the total bay mass were direct outputs of the SEA solver. Figure 10 provides two examples of measured $E_y/P_{in,x}$ spectra compared with FE and SEA model predictions on a 1/3 octave band averaged basis. The data were averaged and 95/50 confidence intervals were calculated among the 5 and 3 drive point locations for central- and side-driven bays, respectively. For these comparisons, in vacuo FE and SEA models were used while experimental total loss factor estimates assigned were as structural loss factors to account for any radiation losses during testing. In general, both FE and SEA results were in agreement with experimental results at all transfer bay locations, especially for locations within the same channel (region between two frames) as the



(a) Free hanging

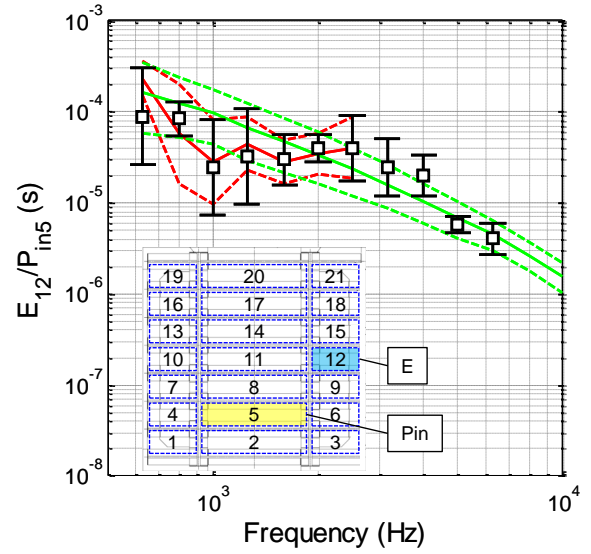


(b) In situ

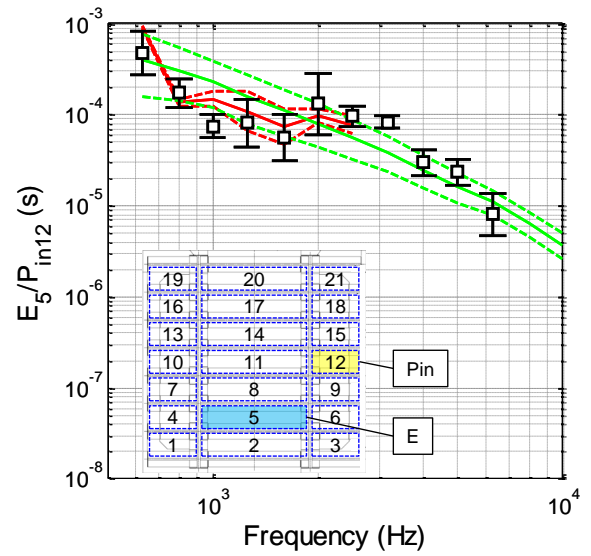
FIGURE 9. Test results vs. FE prediction of response natural frequency and shape MAC value for free hanging and in situ BCs.

driven bay.

The measured DAF TL is shown in figure 11 with predictions from vibroacoustic SEA and FE modal domain analysis methods. The vibroacoustic SEA results are not in good agreement with experimental results, which is attributed to the lumped coincidence frequencies of the smeared bay subsystems. In reality, different coincident frequencies are expected at the substructure flange and thin skin regions as denoted in the figure 11



(a) Center bay driven



(b) Side bay driven

FIGURE 10. Free hanging panel 1/3 octave band averaged E/P_{in} measured results (black squares) compared with FE (red line) and SEA (green line) model predictions for center bay and side bay driven cases. 95/50 confidence intervals shown with bars and dashed lines.

insert. For the vibroacoustic FE method, clamped, in vacuo panel FE modes up to 4 kHz were used for analyses up to the 3150 Hz 1/3 octave band. The acoustic impedance seen on either side of the panel was implemented using the Rayleigh integral formulation, which assumes an infinitely baffled array of pistons radiating into a half space [8], and is given in terms of force/velocity

in the spatial domain as

$$\mathbf{Z}_f = j\omega\rho_0\mathbf{A}^2/(2\pi\mathbf{R})e^{(-jk\mathbf{R})}, \quad (6)$$

where \mathbf{A} is an $N \times N$ diagonal matrix containing nodal areas and \mathbf{R} is the similarly sized nodal separation matrix. To avoid undefined terms, the diagonal of \mathbf{Z}_f was replaced with the expression for the radiation impedance of a baffled piston,

$$Z = \rho_0 c_0 \hat{r}^2 \left((k\hat{r})^2 / 2 + j8k\hat{r} / (3\pi) \right), \quad (7)$$

where \hat{r} is the piston radius chosen to conserve nodal area [9]. The mobility FRF was then evaluated in the modal domain with the expression

$$\mathbf{y} = j\omega (\mathbf{k}_d + j\omega\mathbf{z}_f)^{-1}, \quad (8)$$

where \mathbf{k}_d is the modal domain dynamic stiffness matrix given by

$$k_{d_{mm}} = -\omega^2 + \omega_m^2 (1 + j\eta_m), \quad (9)$$

and where the modal damping and radial eigenfrequencies are denoted as η_m and ω_m , respectively. The $M \times M$ acoustic impedance term in the modal domain is determined from

$$\mathbf{z}_f = \Phi^T \mathbf{Z}_f \Phi, \quad (10)$$

where Φ is the $N \times M$ matrix of included modes. The modal damping values used here were interpolated from the modal curve fit and IRDM results shown in figure 8 with radiation losses subtracted from the TLF in the 630 Hz to 4 kHz 1/3 octave bands where radiation loss results were available. It was noted that the differences between the conditioned loss factor and the TLF were arguably small and that the TLF would have served as an equally viable estimate in this case given the uncertainty in the loss factor estimates.

The modal domain velocity cross power spectral density (CPSD) matrix is then calculated,

$$\mathbf{G}_{vv} = \mathbf{y}\Phi^T \mathbf{G}_{FF} \Phi \mathbf{y}^*, \quad (11)$$

for a given spatial domain force CPSD, \mathbf{G}_{FF} . A DAF force CPSD was applied to the in-plane skin nodes in this way to simulate the incident field seen in the SALT reverb chamber during the TL test and is given as

$$\mathbf{G}_{FF} = \langle G_{pp} \rangle A^2 \text{sinc}(k\mathbf{R}), \quad (12)$$

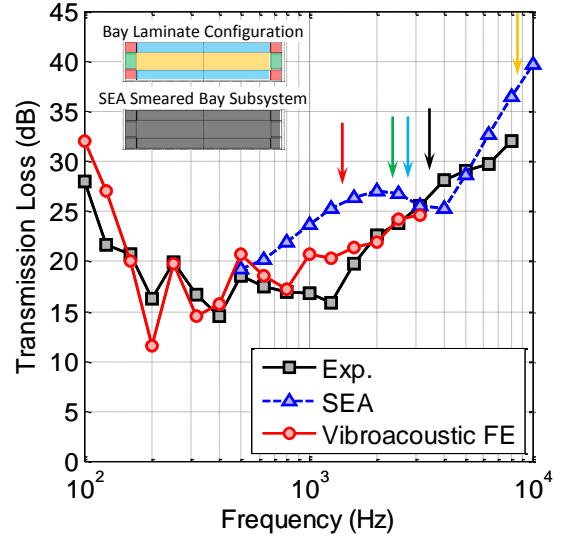


FIGURE 11. Experimental TL compared with vibroacoustic FE and SEA results. The free bending wave critical frequency of the “smeared” SEA bay subsystem (black arrow) is shown in contrast with that of each bay laminate (arrow color denoted in the insert).

where $\langle G_{pp} \rangle$ is the space averaged DAF single point pressure PSD (which was simply set to unity for TL predictions) [10]. The TL is then determined from

$$TL = 10\log_{10} (P_{inc}/P_{rad}), \quad (13)$$

where the incident power is estimated by integrating the random incidence intensity over the wetted surface area S such that [8]

$$P_{inc} = \langle G_{pp} \rangle S / (4\rho_0 c_0). \quad (14)$$

The radiated power was then calculated from the real part of the product of force and velocity summed over all modes,

$$P_{rad} = \sum_{m=1}^M \sum_{m'=1}^M \text{Re}\{z_{f_{mm'}} G_{v_m v_{m'}}\}. \quad (15)$$

FLIGHT CONDITION EVALUATION

Subsequent TL predictions were made using the vibroacoustic FE approach previously described while considering turbulent boundary layer (TBL) excitation as well as 63.4 kPa (9.2 psi) IML side static pressurization to simulate representative cruise flight conditions. For these exploratory analyses, a frequency independent structural loss factor of 1.5% was assumed. The

acoustic wavespeeds and air densities on each wetted side of the panel were adjusted to account for interior and exterior conditions giving 343 m/s, 1.21 kg/m³, and 297 m/s, 0.38 kg/m³, respectively. Low exterior temperature and mean flow aeroelastic effects on the structure were not included in the analysis and were left for future consideration. The model size was reduced by a factor of two along the frame dimension at this point to reduce run times and the near-perimeter laminate pad-ups specific to the test article were also removed from the FE model. The TL bias introduced by the size reduction relative to the full 1.22 m×1.22 m model was within 2 dB in the 400 Hz 1/3 octave band and approached zero with increasing frequency. TBL thickness estimates, shown in figure 13, were supplied from Computational Fluid Dynamics (CFD) analysis of the HWB-450-1L planform [1] and were used to generate the streamwise and cross-stream coherence lengths based on Efimtsov's model [11] at an altitude of 10.7 km at standard atmosphere with a free stream Mach of 0.85 located 20 m from the nose along the centerline. The boundary layer convective velocity, U_c , was assumed to be 70% that of the free stream velocity, U_∞ . Separable Corcos, modified Corcos, and non-separable Mellen elliptical models were considered for the force CPSD matrix formulation [12–14]. The TBL CPSD formulations applied here vary significantly at streamwise wavenumbers below the convective ridge, Corcos being the most conservative with the highest estimate of low wavenumber content followed by the elliptical model and then the modified Corcos. To further illustrate the differences between these models, their normalized wavenumber domain responses evaluated at the 2 kHz 1/3 octave band center frequency are shown in figure 12.

A design modification consisting of a 64% reduction in stringer flange width and a 32% increase in stringer web height was then evaluated relative to the baseline configuration. The modified configuration was relatively lighter by 6.5%. One would expect this modification to reduce the flexural stiffness of local bay modes by increasing the relative thin skin area of the bays while increasing the global mode stiffness parallel with the stringers due to increased web height. Figure 14 shows the insertion loss (change in TL relative to baseline configuration) attributed to the modification for the TBL CPSD formulations considered as well as a DAF. Standard “room” conditions were assumed on both sides of the panel for the DAF case to simulate a typical lab evaluation setting, although IML static pressurization was maintained. Considering DAF excitation, the design modification appears to improve the TL around 2 kHz, which is attributable to reduced bay stiffness and thus reduced bay radiation efficiency. However, in the mid frequencies below ~ 1.6 kHz, the results are mixed and tend toward poorer TL performance likely due to the global wavelength stiffening effects of increased stringer web heights increasing the radiation efficiency.

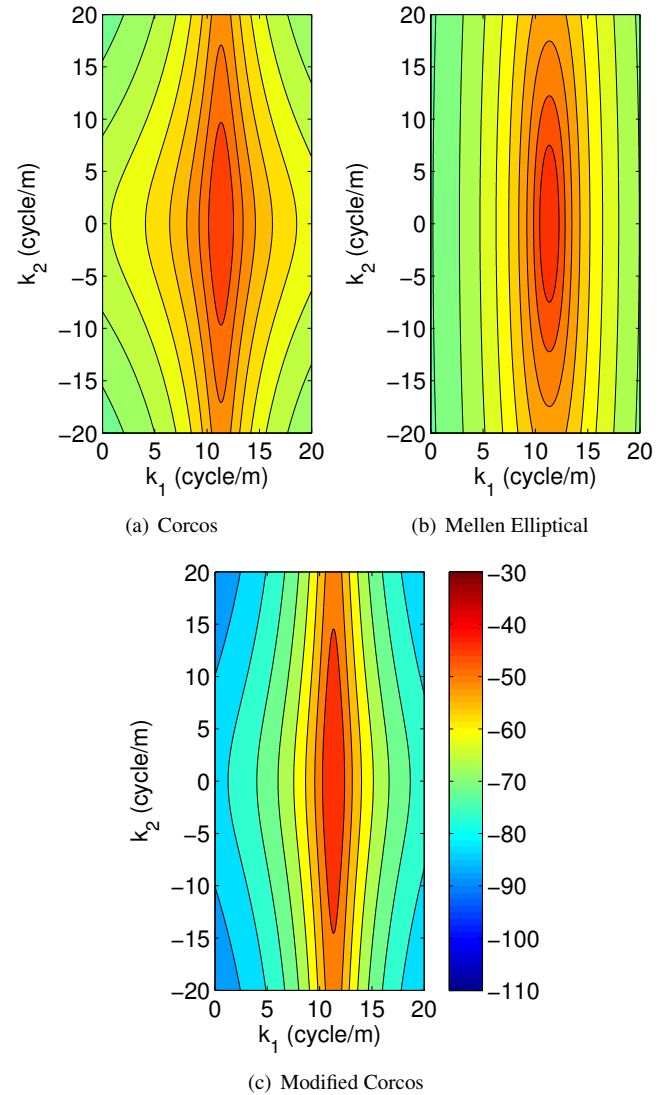


FIGURE 12. Normalized TBL wavenumber spectra (in dB) for the three CPSD models considered plotted along the streamwise k_1 and cross-stream k_2 wavenumbers evaluated at the 2 kHz 1/3 octave band center frequency.

For the TBL excitations considered, a different, but not wholly opposite trend is noticed. Here, the higher bay mobility exhibited by the design modification likely increased the TBL acceptance which negated or overpowered any gains due to reduced radiation efficiency. In an attempt to further illustrate the model differences and why their behaviors diverge when subject to lab DAF and TBL excitations, the wavenumber domain modal sensitivity spectra were calculated for all modes, $\Psi(\mathbf{x})$, within the

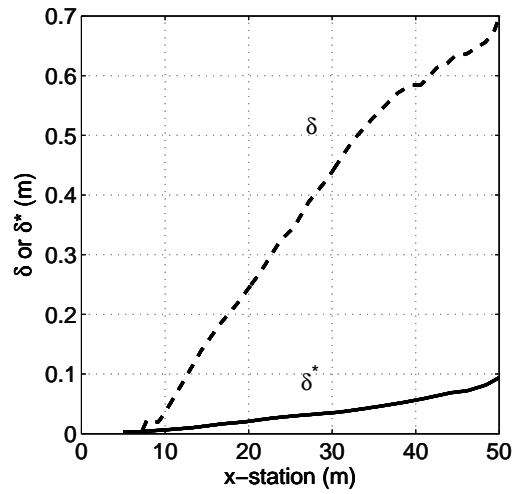


FIGURE 13. CFD estimates of boundary layer thickness (δ) and displacement thickness (δ^*) along the top center-line of the HWB-450-1L planform at mach 0.85 and at an altitude of 10.7 km on a standard day.

2 kHz 1/3 octave band via spatial Fourier transform

$$\Phi_m(\mathbf{k}) = \iint \Psi(\mathbf{x}) e^{j\mathbf{k}\cdot\mathbf{x}} d\mathbf{x}, \quad (16)$$

and then band-summed and normalized by $\sum |\Phi_m(\mathbf{k})|^2 = 1$. The results are plotted in figure 15 along with the TBL convective wavenumber, $k_1 = k_c = \omega/U_c$, and lab condition acoustic wavenumber, $k = \omega/c$, $c = 343$ m/s, evaluated at the 2 kHz 1/3 octave band center frequency. It is apparent that the majority of the 2 kHz 1/3 octave band modal content moves away from the acoustic wavenumber region, which may account for the improved DAF behavior of the design modification. On the contrary, the content tends toward the TBL convective ridge in the streamwise direction, which could account for the reduced performance when TBL excitation is considered.

SUMMARY AND CONCLUSIONS

A PRSEUS baseline configuration test article was constructed and subjected to a suite of tests. FE and SEA models were developed and correlated with the experimental results. The FE model was in good agreement with test results on the basis of low frequency mode shape correlation for unconstrained BCs. Clamped BCs were found to represent the experimental in situ BC fairly well, although a slight bias introduced with this assumption was noted, especially in the lower frequencies where facility interaction was evident. At higher frequencies, structural vibration correlations were performed on the basis of bay vibra-

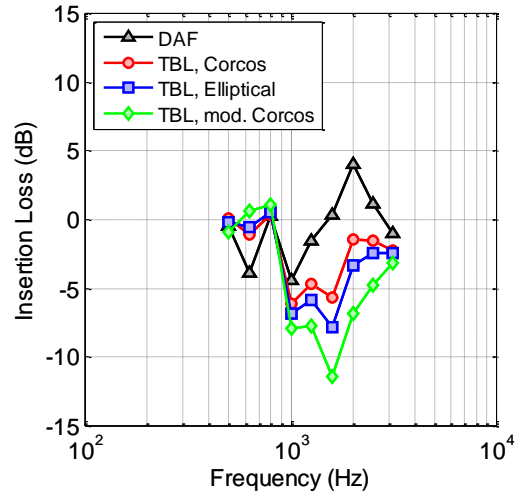


FIGURE 14. Insertion loss attributed to design modification for DAF and three TBL CPSD formulations (Efimtsov coherence length model used in all TBL cases).

tional energy content relative to point excitation power input. In this case, both FE and SEA results were in fairly good agreement for their respective frequency ranges of application. TL comparisons between experiment and vibroacoustic FE results were generally good showing deviations within 5 dB. Much of the deviation was arguably due to uncertainties in the measured total and radiation loss factors, especially around 1 kHz. The vibroacoustic SEA model performed per design. It exhibited a lumped acoustic coincidence near 3.5 kHz – an artifact of smearing the flange and skin details into a uniform SEA plate subsystem. For larger, systemic fuselage models requiring an efficient SEA (or similar) approach, the authors believe it would be better to use a hybrid modeling approach where the vibroacoustic coupling loss factors of representative regions are evaluated deterministically and then applied to subsystems in the SEA model. Finally, the IL attributed to a conceptual modification was shown for representative flight condition pressurization and boundary layer excitation at a region 20 m from the nose of the aircraft. The results suggested that basing design changes on DAF trade studies may not be applicable for representative flight conditions where the TBL is the primary source of excitation. The differences between the two types of excitation were found to not be easily discernable in a straightforward, *a priori* manner and depended on the frequency dependant wavelength characteristics of the particular structure under study. Furthermore, the TBL CPSD formulations applied here varied for the most part in the low wavenumber region below the convective ridge and were found to affect not only the TL, but also the IL, which may be of concern when considering an optimization procedure where relative changes in TL constitute the metric of fitness.

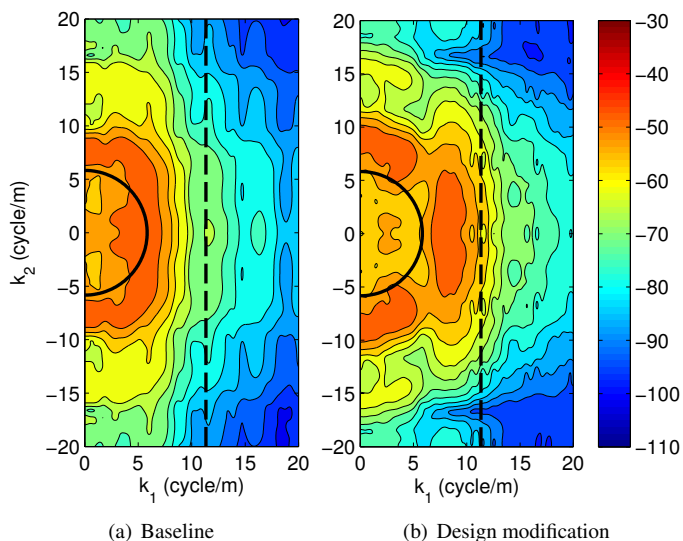


FIGURE 15. Modal sensitivity content (summed within the 2 kHz 1/3 octave band and normalized) for the baseline and modified designs plotted in dB along the streamwise k_1 and cross-stream k_2 wavenumbers. Also shown are the TBL convective wavenumber (- -) and lab condition acoustic wavenumber (—) evaluated at the 2 kHz 1/3 octave band center frequency

ACKNOWLEDGMENT

We gratefully acknowledge The Boeing Company for manufacturing the test article and providing CFD boundary layer characteristics.

REFERENCES

- [1] Alex Velicki et al. PRSEUS Acoustic Panel Fabrication. Technical Report CR 217309, NASA, 2011.
- [2] Ferdinand W. Grosveld. Calibration of the Structural Acoustics Loads and Transmission facility at NASA Langley Research Center". In *Proceedings of the Internoise 1999 meeting*, Fort Lauderdale, FL, December 1999.
- [3] Ferdinand W. Grosveld. Characterization of the Reverberation Chamber at the NASA Langley Structural Acoustics Loads and Transmission (SALT) Facility. Technical Report CR (pending), NASA, 2012.
- [4] ASTM E 2249. *Standard Test Method for Laboratory Measurement of Airborne Transmission Loss of Building Partitions and Elements Using Sound Intensity*, 2002.
- [5] Brandon C. Bloss and Mohan D. Rao. Estimation of frequency-averaged loss factors by the power injection and the impulse response decay methods. *Journal of the Acoustical Society of America*, 117(1):240–249, January 2005.
- [6] Ran Cabell et al. Loss factor estimation using the impulse response decay method on a stiffened structure. In *Proceedings of Inter-noise 2009*, Ottawa, Canada, August 2008.
- [7] Finn Jacobsen. *The sound field in a reverberation room*. Technical University of Denmark, Lyngby, Denmark, 2011.
- [8] Frank Fahy. *Sound and Structural Vibration: Radiation, Transmission, and Response*. Academic Press, 2007.
- [9] Allan D. Pierce. *Acoustics: An Introduction to Its Physical Principles and Applications*. Acoustical Society of America, 1991.
- [10] Richard K. Cook, R. V. Waterhouse, R. D. Berendt, Seymour Edelman, and Jr. M. C. Thompson. Measurement of correlation coefficients in reverberant sound fields. *Journal of the Acoustical Society of America*, 27(6):1072–1077, November 1955.
- [11] B. M. Efimtsov. Characteristics of the field of turbulent wall pressure fluctuations at large Reynolds numbers. *Akusticheskii Zhurnal*, 28:491–497, July 1982.
- [12] G. M. Corcos. Resolution of pressure in turbulence. *Journal of the Acoustical Society of America*, 35(2):192–199, February 1963.
- [13] Y. F. Hwang. A discrete model of turbulence loading function for computation of flow-induced vibration and noise. In *Proceedings of the ASME International Mechanical Engineering Congress and Exposition*, Anaheim, CA, November 1998.
- [14] R. H. Mellen. Wave-vector filter analysis of turbulent flow. *Journal of the Acoustical Society of America*, 95(3):1671–1673, March 1994.